IAA-AAS-DyCoSS2-14 10-03

SUN-HEADING ESTIMATION USING A PARTIALLY UNDERDETERMINED SET OF COARSE SUN SENSORS

Stephen A. O'Keefe* **and Hanspeter Schaub†**

A comparison of several different methods to estimate the sun direction vector using a partially underdetermined set of cosine-type coarse sun sensors is presented. These methods are used in conjunction with a control law to reorient a spacecraft to a power positive orientation. Coarse sun sensors are commonly used to perform coarse attitude determination and accurately point a spacecraft's solar arrays at the Sun. These sensors are attractive due to their relative inexpensiveness, small size, and reduced power consumption. This paper presents four methods for accurately solving for the sun direction vector with decreased sensor requirements, the first is a simple weighted average method, the second and third are variations on a combination of least squares and minimum norm criteria, and the final leverages an extended Kalman filter approach. All four methods are combined with a control law and shown through numerical simulation to be capable of reorienting the spacecraft from any initially unknown attitude to a power positive state in a matter of minutes. The extended Kalman filter method is shown to provide the most accurate estimate of the sun heading direction, but the weighted least squares minimum norm solution provides the fastest convergence when no angular velocity measurements are available.

INTRODUCTION

In recent years there has been a significant increase in interest in smaller satellites as lower cost alternative to traditional satellites, particularly with the rise of the CubeSat.[1] While these small satellites often use the latest advanced technology in their subsystems, there is a noticeable lag in the development of attitude control subsystems.[2] And due to stringent mass, size, and often budget constraints placed on these satellites they typically rely on simple sensor hardware such as coarse sun sensors and magnetometers.

These spacecraft commonly use a number of sun sensors to determine the sun direction vector in the body frame. High accuracy sun sensors often combine multiple measurements[3] or use charge-couple-devices (CCDs)[4] to determine the direction of the Sun. These digital sensors output a vector observation of the sun direction and two or more such vector observations are combined to deterministically solve for the true sun direction. Many methods exist for solving such a problem including TRIAD,[5] Davenport's Q-Method,[6] QUEST,[7] FOAM,[8] and OLAE.[9]

Alternatively, cosine-type coarse sun sensors (CSS) output a voltage relative to the input light and are attractive due to their inexpensiveness, small size, and minimal power consumption. These sensors are often used, in concert with other sensors,[10,11] during deployment to accurately point the spacecraft's solar arrays at the Sun to achieve power positiveness or to perform coarse attitude

*Graduate Student, Aerospace Engineering Sciences, University of Colorado, Boulder, CO
†Professor, Aerospace Engineering Sciences, University of Colorado, Boulder, CO

determination. Unfortunately, these cosine-type CSS output a scalar measurement, not a vector observation, and so deterministic methods that rely on multiple vector observation are not usable.

Instead, the sun direction vector must be determined through the use of deterministic single-point methods or statistical filtering algorithms. A spacecraft's attitude can generally be determined geometrically at any particular time if the Sun is simultaneously in the field of view of at least three cosine-type sensors; a more reliable estimate is found if continuous 4π steradian coverage is achieved by a minimum of four sensors. Statistical filtering algorithms provide an estimate of the spacecraft's attitude based on a collection of measurements over time. In particular, sequential filtering algorithms process measurements as soon as they are received and are commonly derived from the Kalman filter[12] which produces a statistically optimal estimate for linear systems. The Kalman filter assumes a linear dynamical system and many variants have been developed for non-linear systems, the most popular variant is the extended Kalman filter[13] (EKF) which linearizes the nonlinear system about the current estimate.

Because CSS are relatively inexpensive, it is not uncommon for spacecraft to have a multitude of sensors placed around the exterior to achieve the coverage required for determining the sun direction geometrically. The addition of so many sensors to the spacecraft is not without hazards. The fields of view of the CSS can become blocked by other instrumentation, the CSS can interfere with other payloads, cabling must be routed for all sensors, and extra sensors will require additional testing time and complexity. The placement of these sensors is generally an iterative process based on experience and prior designs, but can be optimized through various methods.[14,15]

If, however, it is unfeasible to use a large number of CSS or additional instrumentation, due to budgetary, power, or space constraints, and the spacecraft must still accurately orient its solar arrays at the Sun following deployment, an alternative method is proposed. The sun direction is not needed initially to high precision in order for the spacecraft to maneuver to a sun pointing orientation. In fact, a full three-degree of freedom description is not needed as rotation about the solar array normal vector will not negatively impact power generation. In this situation lower fidelity estimates of the sun direction are enough for a control law to begin reorienting the spacecraft using reaction wheels or thrusters. Therefore, fewer sensors are needed in regions far from the desired pointing vector and the total number of sensors required can be reduced. Once the spacecraft begins to reorient, more sensors oriented along the desired alignment axis help to refine the estimate of the sun direction vector and accurately point the spacecraft's solar arrays at the Sun. While it may not be possible to uniquely determine geometrically the location of the Sun direction at each time step in the underdetermined case, the time histories of measurements from several CSS can be combined in an estimation filter to determine the sun direction vector. Once the spacecraft is pointing at the Sun and generating power, more accurate measurement sensors, such as star trackers, can be turned on to determine the spacecraft's absolute attitude.

This paper examines using CSS in a partially underdetermined configuration, both solely and in concert with a rate gyroscope, to orient a spacecraft's solar arrays at the Sun following deployment to determine how well low cost sensors can be used to maintain high performance. A comparison is made between a simple weighted average approach, a least squares minimum norm solution, and an extended Kalman filter approach which incorporates time histories of measurements into the estimate. First, a description of the sensors and the spacecraft configuration used are presented. A basic weighted average (WAVG) method of determining the sun direction unit vector is detailed followed by least squares minimum norm method (LSMN), a weighted LSMN (WLSMN) method, and an EKF formulation. Finally, numerical simulation results demonstrating the performance of

each approach are presented.

COSINE SUN SENSOR MEASUREMENT MODEL

The cosine-type CSS used in this study are composed of photodiodes with a glass cover for filtering out undesired wavelengths and optionally baffles for restricting the field of view. Assuming Lambert's cosine law the solar flux F_i, in W/m^2, that impacts the ith CSS due to the direct solar flux of the Sun $F_\odot$ is given by[16]

$$F_{d_i} = F_\odot \left(\boldsymbol{n}_i \cdot \boldsymbol{s} \right) + \eta_i \tag{1}$$

where $\boldsymbol{n}_i$ is the unit normal of the ith CSS, $\boldsymbol{s}$ is the unit direction vector form the spacecraft to the Sun, and η_i is zero mean Gaussian noise. The typical unit vector notation $\hat{\cdot}$ has been omitted to avoid confusion later when it is used to denote an estimate.

In practice the output voltage of the ith CSS is assumed proportional to the input flux through the relation

$$V_i = C_i \left(\boldsymbol{n}_i \cdot \boldsymbol{s} \right) + \eta_i \tag{2}$$

where the proportionality constant

$$C_i = \frac{V_{i_{\max}}}{F_{\text{cal}}} F_\odot \tag{3}$$

is determined during ground testing using a calibration flux F_{cal}. Ideally this calibration flux will equal the flux due to direct sunlight on orbit $F_\odot$, but any ground-based testing of this calibration parameter for a particular CSS will have to account for the atmospheric reduction of the solar irradiance received. While estimates are available for how much stronger the solar irradiance will be in space, a CSS algorithm that is insensitive to this calibration parameter will enable significantly simpler, and thus cheaper, CSS calibration and testing procedures.

Earth Albedo Model

Solar radiation that impacts the Earth is partially absorbed, partially specularly reflected, and partially diffusely reflected. Cosine-type CSS are sensitive to any light and on orbit the most significant light source other than direct sunlight is light from the Sun diffusely reflected by the Earth. Solar radiation that is absorbed by the Earth and later radiated at infrared wavelengths is easily filtered through mechanical means and the energy due to specular reflectance is generally small and ignored.[17]

The sunlight diffusely reflected by the Earth is a function of latitude, longitude, and the ambient reflectivity of the Earth that varies with ground cover and atmospheric conditions. Again assuming a Lambertian cosine law, the flux seen by the ith CSS due to the diffuse reflectance of the Earth is modeled as[10]

$$F_{\alpha_i} = \frac{F_\odot}{\pi} \int_{\boldsymbol{A}} \frac{\alpha}{\|\boldsymbol{r}_{AB}\|^2} \left(\boldsymbol{n}_A \cdot \boldsymbol{s}_E \right) \left(\boldsymbol{n}_A \cdot \frac{\boldsymbol{r}_{AB}}{\|\boldsymbol{r}_{AB}\|} \right) \left(\frac{\boldsymbol{r}_{AB}}{\|\boldsymbol{r}_{AB}\|} \cdot \boldsymbol{n}_i \right) dA \tag{4}$$

where $F_\odot$ is the solar irradiance in the vicinity of the Earth; $\boldsymbol{A}$ is the surface of the Earth visible to the spacecraft, $(\boldsymbol{n}_A \cdot \boldsymbol{r}_{AB}) > 0$ and $(\boldsymbol{r}_{AB} \cdot \boldsymbol{n}_i) \geq \cos\left(\text{FOV}_i\right)$, that is also illuminated, $(\boldsymbol{n}_A \cdot \boldsymbol{s}_E) > 0$; $\boldsymbol{n}_A$ is the unit normal of an incremental area on the surface of the Earth; $\boldsymbol{s}_E$ is the unit direction vector from the Earth to the Sun; $\boldsymbol{r}_{AB}$ is a vector from an incremental area on the surface of the Earth to the body of the spacecraft; and α is the albedo constant of the incremental area.

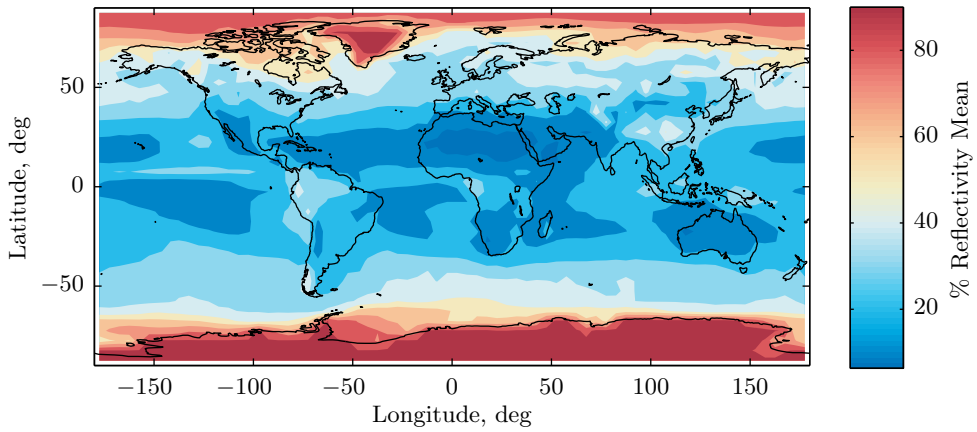

(a) Mean reflectivity.

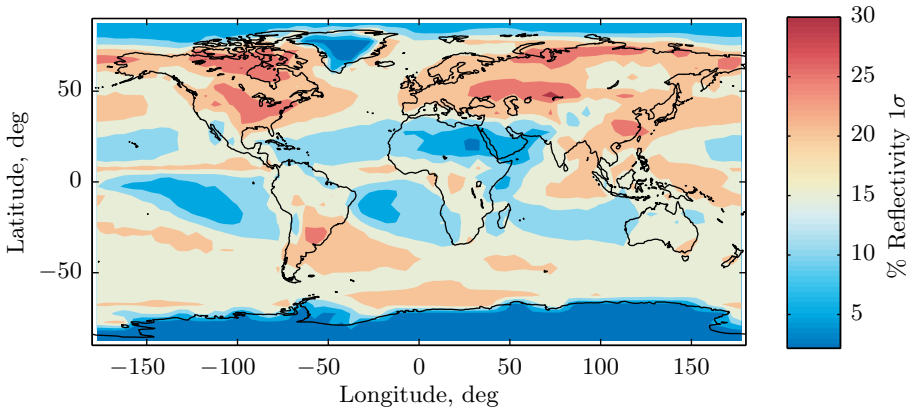

(b) Standard deviation of reflectivity.

Figure 1: Mean and standard deviation of the reflectivity of Earth as measured by TOMS mission between 2000 and 2005 used in numerical simulations.

For this work the albedo constant for the Earth is taken from the NASA Total Ozone Mapping Spectrometer mission data. The data used in this effort were acquired as part of the activities of NASA's Science Mission Directorate, and are archived and distributed by the Goddard Earth Sciences (GES) Data and Information Services Center (DISC). Daily measurements on a $5\,\text{deg} \times 5\,\text{deg}$ latitude longitude grid from 2000 to 2005 are used to generate mean and standard deviations for the reflectivity of Earth. These values are shown, with global coastlines superimposed for reference, in Figure 1. Bhanderi has shown that the irradiance due to be albedo can be anywhere between 0% and $\sim$50% of the incident solar irradiance with maximum albedo not over the poles, but over Greenland during local summer at noon.[18]

Using the Earth albedo model, the output voltage of the ith given in Equation (2) is modified as

$$V_i = C_i \left((\boldsymbol{n}_i \cdot \boldsymbol{s}) + \frac{F_{\alpha_i}}{F_\odot} \right) + \eta_i \tag{5}$$

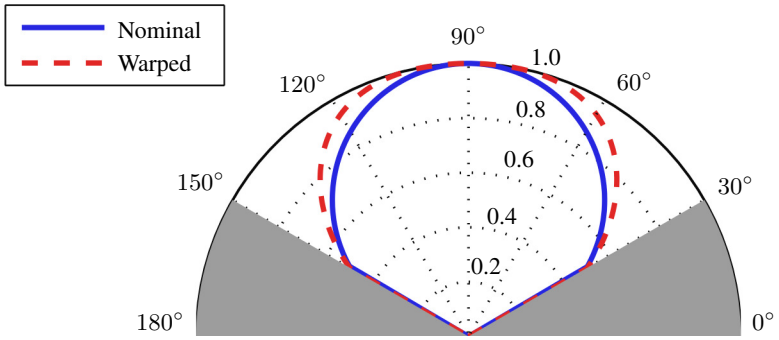

Figure 2: Illustration of CSS field of view and flattened peak response.

where the proportionality constant remains as shown in Equation (3).

CSS Measurement Error Sources

Many commercially available photodiodes do not exhibit the precise cosine response modeled by Equation (1). Commonly, actual voltage measurements $\tilde{V}_i$ from photodiodes exhibit a more flattened peak response approximated by

$$\tilde{V}_i = V_i \left(1 + \frac{1}{2}\beta^2 - 0.65\beta^4\right) \tag{6}$$

where V_i is the ideal output of the ith sensor and $\beta = \sin\left(\cos^{-1} V_i\right)$. This warping can cause a difference in the output of a sensor by as much as 8% and is shown in Figure 2. It is usually calibrated out during ground testing, but is used here to simulate poor or no calibration, a possibility for small satellite programs with limited ground test funding.

CSS Configuration

The spacecraft used for this study is assumed to be equipped with eight cosine-type CSS in a dual pyramid configuration. Four sensors with 120 deg edge-to-edge fields of view are arranged on the $+z$ and $-z$ faces of the spacecraft oriented 90 deg apart and angled 45 deg from the body z axis. An illustration of this configuration is shown in Figure 3a.

Figure 3b shows the number of CSS to which the Sun is visible for any relation of the Sun with respect to the spacecraft. This figure takes into account that the fields of view of the CSS are clipped at the local-horizontal plane by the spacecraft structure and solar panel arrays; a CSS cannot see the Sun when it is below the local (x, y) plane. A Lambert cylindrical area preserving projection is used so as to give a fair comparison of the over, uniquely, and underdetermined areas of coverage.

Multiple sensor coverage is provided along, $+z$, and opposite, $-z$, the solar array normal direction with minimal coverage along the equator of the spacecraft. This configuration leaves the sides of the spacecraft clear for scientific instrumentation and seeks to minimize both the CSS obstruction due to the solar arrays and the amount of internal cabling necessary for the sensors. For this study it is assumed if the solar array normal vector is within 30 deg of the sun direction vector the spacecraft is in a power positive state, generating sufficient power to operate all instrumentation and recharge batteries.

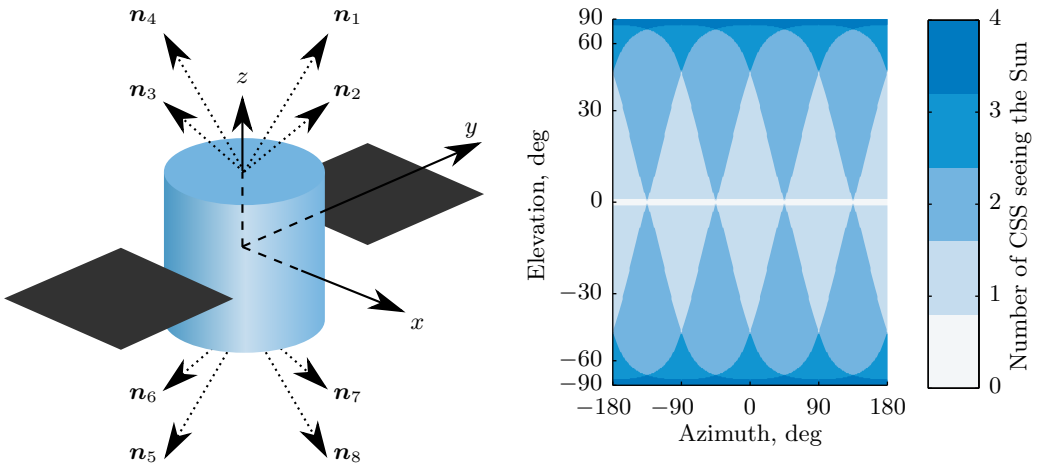

(a) Schematic of spacecraft, $\theta = 45$ deg.

(b) CSS coverage map.

Figure 3: Illustration of spacecraft with CSS unit vectors $\boldsymbol{n}_i$ for a dual pyramid configuration and the associated CSS coverage map shown on a Lambert cylindrical projection.

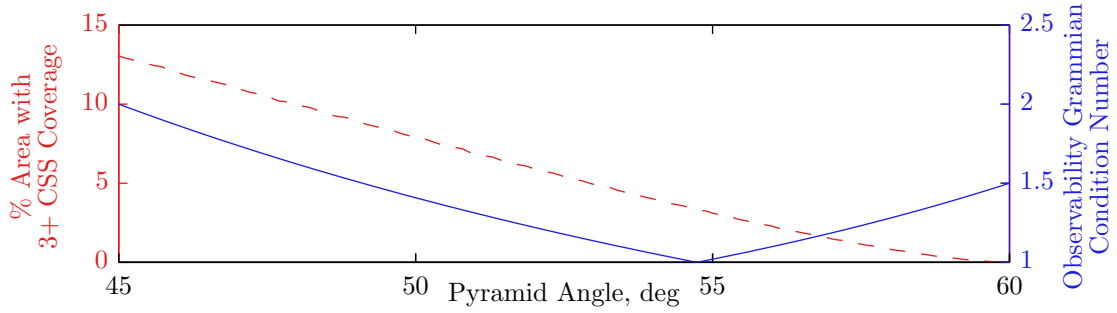

Figure 4: Criteria used for selecting CSS pyramid angle.

Assuming the solar array normals are aligned with the body z axis and using a dual pyramid configuration, the angle θ between the CSS normal vectors and the body z axis should be between 45 deg and 60 deg. Too small of an angle $\theta < 45$ deg results in areas without any sensor coverage near the $x-y$ horizon. Too large of an angle $\theta \geq 60$ deg results in areas without any sensor coverage near the $\pm z$ poles and 4π steradian coverage by at most two sensors.

For the single-point methods that follow, the optimum angle maximizes the area covered by three or more sensors; at $\theta = 45$ deg, 1.64 sr (13%) of the attitude sphere is covered by three or more CSS. For the EKF method the optimum angle minimizes the condition number of the observability Gramian*; at $\theta = 54.7$ deg the condition number reaches a minimum very close to unity. Unfortunately, at $\theta = 54.7$ deg only 0.44 sr (3.5%) of the attitude sphere is covered by three or more CSS, whereas at $\theta = 45$ deg the impact to observability is not nearly as significant. An angle of 45 deg is chosen as it is optimum for the WAVG and LSMN methods, does not significantly negatively impact the observability for the EKF solution, and provides the most redundant coverage

*The degree of observability is measured by the closeness of the condition number of the observability Gramian to unity.

to help alleviate concerns regarding sensor failures.

SUN HEADING ESTIMATORS

Two classes of sun heading estimators are examined here: deterministic single-point methods and filtering algorithms. Deterministic single-point methods use sensor measurements available at a specific time while filtering algorithms combine sensor measurements over a continuous range of time with a dynamic model to estimate the sun direction. Since the underdetermined case is of interest here all of the estimators investigated must be capable of producing an estimate of the sun direction vector when the Sun is only observed by one or two sensors. The first method examined is a single-point approach based on taking the weighted average of all CSS measurements at a given time. A more mathematically robust, but also more complicated, single-point method is examined next which combines a least squares estimate and a minimum norm estimate based on the number of sensor measurements available. This second method is then expanded to include a weighting matrix to better reject noise. Finally, a filtering approach based on an extended Kalman filter is developed.

Weighted Average (WAVG) Method

A simple deterministic estimate for the sun direction vector is formed by taking a weighted average of all the CSS capable of seeing the Sun using

$$^{\mathcal{B}}\hat{\boldsymbol{s}} = \frac{\sum_{i=1}^{N} V_i {}^{\mathcal{B}}\boldsymbol{n}_i}{\|\sum_{i=1}^{N} V_i {}^{\mathcal{B}}\boldsymbol{n}_i\|} \tag{7}$$

where N is the total number of sensors and V_i is the magnitude of the output of the ith sensor given by Equation (2). The matrix $^{\mathcal{B}}\hat{\boldsymbol{s}}$ contains the body frame $\mathcal{B}$ vector components of the best estimate of the sun heading vector $\boldsymbol{s}$. Since the weighted average method represents a deterministic approach, the error of this method is easily calculated for any orientation of the Sun relative to the spacecraft; the resulting error map is shown in Figure 5.

Figure 5 shows a large band near the equator of the spacecraft in which the error is greater than 30 deg. If the Sun is within this region, it will result in a large estimation error, but even an approximate sun heading estimate provides enough knowledge for a controller to apply the appropriate rotation rate. The coverage at the poles is more important. The desired attitude of the spacecraft requires the sun direction vector be aligned with the z axis, and within 19 deg of this axis the error remains less than 10 deg. Thus, the control becomes more precise near the goal orientation.

This weighted average method is attractive as it is computationally simple, provides an error measure when only one sensor is seeing the Sun, and is capable of estimating the sun direction vector to within a few degrees using the configuration described previously.

Least Squares Minimum Norm (LSMN) Method

A more mathematically robust method is the Least Squares Minimum Norm method which combines two methods, least squares and minimum norm, based on the number of CSS measurements available. When the number of measurements available is equal to or greater than three the least squares method is used, and when the system is underdetermined the minimum norm criteria is used.

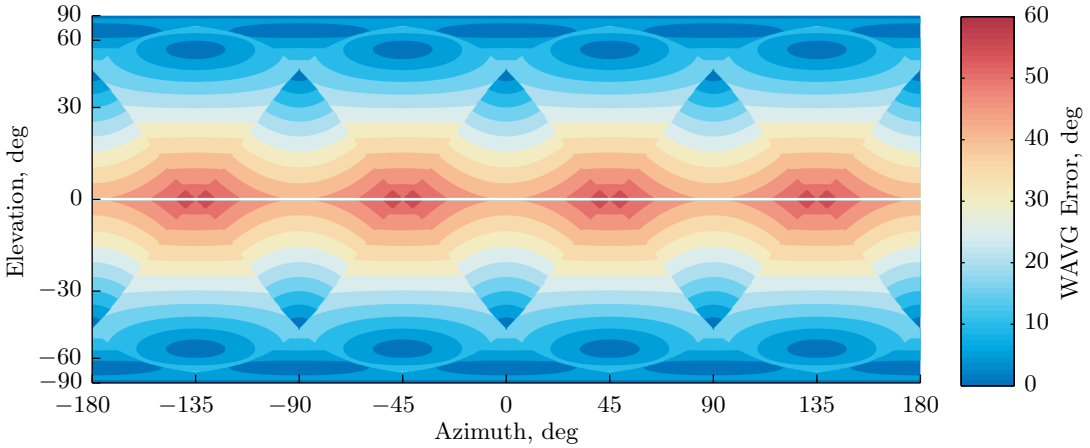

Figure 5: Weighted average method error map for any relation of the Sun with respect to the spacecraft shown on a Lambert cylindrical projection.

Assuming that the flux seen by a CSS due to Earth albedo is treated as noise and the calibration coefficient C_i is the same for all CSS, the measurement of the ith CSS is modeled as

$$\tilde{y}_i = V_i + \eta_i = C\left(\boldsymbol{n}_i \cdot \boldsymbol{s}\right) + \eta_i \tag{8}$$

where η_i is the measurement error for the ith CSS. Here it is assumed that all CSS have been calibrated on the ground to have similar output profiles in response to atmospheric sunlight, and C is the calibration parameter that will scale the CSS performance for space-based operation. This is written in matrix form for all sensors as

$$\begin{bmatrix} \tilde{y}_1 \\ \vdots \\ \tilde{y}_N \end{bmatrix} = \begin{bmatrix} \boldsymbol{n}_1^T \\ \vdots \\ \boldsymbol{n}_N^T \end{bmatrix} \left[C\boldsymbol{s}\right] + \begin{bmatrix} \eta_1 \\ \vdots \\ \eta_N \end{bmatrix} \tag{9}$$

$$\tilde{\boldsymbol{y}} = \boldsymbol{H}\boldsymbol{x} + \boldsymbol{\eta} \tag{10}$$

where $\tilde{\boldsymbol{y}}$ is a vector of measured values, $\boldsymbol{H}$ is a mapping matrix, $\boldsymbol{x}$ is the state vector composed of the linear combination of the calibration coefficient C and the sun direction vector $\boldsymbol{s}$, and $\boldsymbol{\eta}$ is a vector of measurement errors. The elegant blending of C and $\boldsymbol{s}$ into a single state quantity leads to a rigorously linear system. If the number of measurements exceed the dimension of the state vector and $\boldsymbol{\eta} = 0$, the best estimate of the state is given by the least squares solution[19]

$$\hat{\boldsymbol{x}} = \left(\boldsymbol{H}^T\boldsymbol{H}\right)^{-1}\boldsymbol{H}^T\tilde{\boldsymbol{y}}. \tag{11}$$

The sun direction unit vector $\boldsymbol{s}$ is then determined from the state vector through a simple normalization. Note that this process is thus insensitive to the common calibration parameter C making the method robust to incorrect modeling of the expected solar irradiance on-orbit. If, however, there are not enough observations the system is underdetermined and the minimum norm criterion

$$\hat{\boldsymbol{x}} = \boldsymbol{H}^T\left(\boldsymbol{H}\boldsymbol{H}^T\right)^{-1}\tilde{\boldsymbol{y}} \tag{12}$$

is used to determine a unique solution.[19]

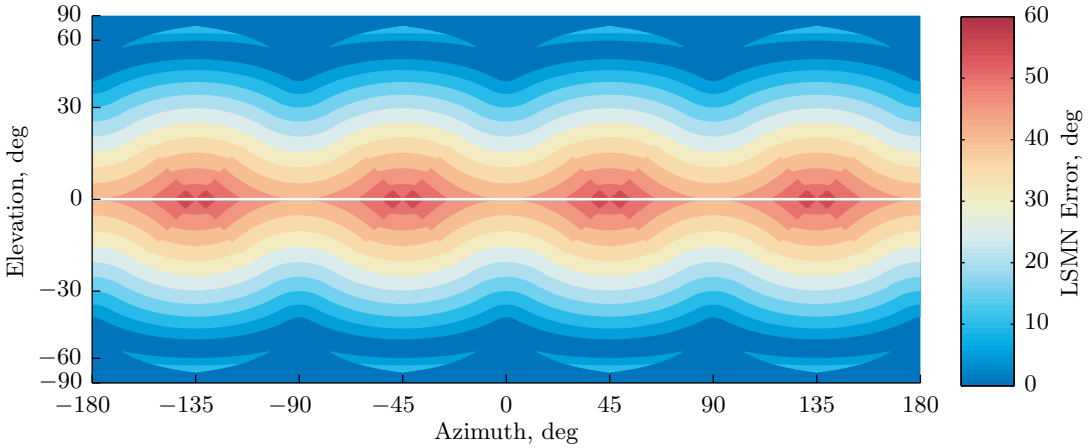

Figure 6: Least Squares Minimum Norm method error map for any relation of the Sun with respect to the spacecraft shown on a Lambert cylindrical projection.

The error of the LSMN method is easily calculated for any orientation of the Sun relative to the spacecraft and is shown in Figure 6. Comparing Figure 5 and Figure 6 it can be seen that the least squares minimum norm estimate has an error that is equal to or less than the weighted average method for all orientations and particularly less in regions of two or three sensor coverage. The LSMN method is slightly more mathematically demanding, requiring the inversion of either a 2×2 or 3×3 matrix, but these calculations do not represent a significant computational burden.

Weighted Least Squares Minimum Norm (WLSMN) Method

As noted previously, the CSS used in this study have a field of view of $120\,\text{deg}$. Therefore, direct sunlight measurements will exhibit a discontinuity as the angle between the normal of the ith CSS and the sun heading vector increases beyond $60\,\text{deg}$. From Equation (2) it is expected that the voltage output of the ith CSS taking into account direct sunlight only to be in the range $0.5C_i < V_i \leq C_i$. Contrarily, the voltage output of the ith CSS due to Earth's albedo can and will be lower than $0.5C_i$.

The Least Squares Minimum Norm method described in the previous section is found in practice to exhibit poor performance when the ratio between the voltage due to direct sunlight and the voltage due to Earth's albedo is large. The weighted least squares solution is given by[19]

$$\hat{\boldsymbol{s}} = \left(\boldsymbol{H}^T \boldsymbol{W} \boldsymbol{H}\right)^{-1} \boldsymbol{H}^T \boldsymbol{W} \tilde{\boldsymbol{y}} \tag{13}$$

and is analogous to the least squares solution in Equation (11). It is found that setting the weights of the individual CSS equal to their output voltage alleviates the errors seen in the LSMN method due to low input voltages due to Earth's albedo and does not impact the nominal error map. This modified method retains the desirable property of being robust to uncertainties in the solar irradiance seen on-orbit versus that seen during ground testing.

Extended Kalman Filter (EKF) Method

A common attitude estimation problem involves propagating the state dynamics and correcting that estimate using a direct measurement of the body's attitude. Thus, instead of solving the geom-

etry of the CSS measurement values at any instant in time, a time history of sensor output is used to correct an estimate of the sun vector being propagated. As noted previously, if the true sun vector lies in a region where only single sensor coverage exists the estimate is significantly in error. A filtering approach overcomes these regions of unobservability through the accumulation of multiple measurements over time. The following section describes the application of a continuous-discrete extended Kalman Filter to the problem of estimating the sun direction unit vector in the spacecraft body frame. At first, it is assumed that the angular velocity of the spacecraft $\boldsymbol{\omega}$ is determined via a rate gyroscope.

The continuous-time state dynamics model for a nonlinear system is given by

$$\dot{\boldsymbol{x}}(t) = \boldsymbol{f}(\boldsymbol{x}(t), \boldsymbol{u}(t), t) + \boldsymbol{g}(\boldsymbol{x}(t), \boldsymbol{w}(t), t) \tag{14}$$

with discrete-time measurements given by

$$\tilde{\boldsymbol{y}}_k = \boldsymbol{h}(\boldsymbol{x}_k) + \boldsymbol{v}_k \tag{15}$$

where $\boldsymbol{x}$ is the state vector, $\boldsymbol{f}$ represents the system dynamics, $\boldsymbol{u}$ is the control input, $\boldsymbol{g}$ is a process noise function, $\boldsymbol{w}(t) \sim N(\boldsymbol{0}, \boldsymbol{Q}(t))$ is the process noise, $\tilde{\boldsymbol{y}}_k$ is the measurement vector available at t_k, and $\boldsymbol{v}_k \sim N(\boldsymbol{0}, \boldsymbol{R})$ is the measurement noise.

The extended Kalman filter operates as a "predictor-corrector" algorithm where the state and covariance are first propagated, denoted by a superscript $-$, using the state dynamics model and then updated, denoted by a superscript $+$, when measurements are available. The state and covariance estimates, $\hat{\boldsymbol{x}}$ and $\hat{\boldsymbol{P}}$, are initialized using

$$\hat{\boldsymbol{x}}\left(t_0\right) = \hat{\boldsymbol{x}}_0 \tag{16}$$

$$\hat{\boldsymbol{P}}\left(t_0\right) = E\left\{\hat{\boldsymbol{x}}_0 \hat{\boldsymbol{x}}_0^T\right\} \tag{17}$$

where E is the expected value operator. The state and covariance are propagated until the time of the next available measurement using the state dynamics

$$\dot{\hat{\boldsymbol{x}}}(t) = \boldsymbol{f}(\hat{\boldsymbol{x}}(t), \boldsymbol{u}(t), t) \tag{18}$$

and the continuous-time Lyapunov differential equation[20]

$$\dot{\hat{\boldsymbol{P}}}(t) = \boldsymbol{F}\hat{\boldsymbol{P}}(t) + \hat{\boldsymbol{P}}(t)\boldsymbol{F}^T + \boldsymbol{G}\boldsymbol{Q}(t)\boldsymbol{G}^T \tag{19}$$

where

$$\boldsymbol{F} \equiv \left.\frac{\partial \boldsymbol{f}}{\partial \boldsymbol{x}}\right|_{\hat{\boldsymbol{x}}(t), \boldsymbol{u}(t)}, \quad \boldsymbol{G} \equiv \left.\frac{\partial \boldsymbol{g}}{\partial \boldsymbol{w}}\right|_{\hat{\boldsymbol{x}}_k, \boldsymbol{w}=0}. \tag{20}$$

The propagated state $\hat{\boldsymbol{x}}_k^-$ and covariance $\hat{\boldsymbol{P}}_k^-$ are finally updated with the latest measurement information using[20]

$$\boldsymbol{H}_k(\hat{\boldsymbol{x}}_k^-) \equiv \left.\frac{\partial \boldsymbol{h}}{\partial \boldsymbol{x}}\right|_{\hat{\boldsymbol{x}}_k^-} \tag{21}$$

$$\boldsymbol{K}_k = \hat{\boldsymbol{P}}_k^- \boldsymbol{H}_k^T(\hat{\boldsymbol{x}}_k^-)\left[\boldsymbol{H}_k(\hat{\boldsymbol{x}}_k^-)\hat{\boldsymbol{P}}_k^- \boldsymbol{H}_k^T(\hat{\boldsymbol{x}}_k^-) + \boldsymbol{R}_k\right]^{-1} \tag{22}$$

$$\hat{\boldsymbol{x}}_k^+ = \hat{\boldsymbol{x}}_k^- + \boldsymbol{K}_k\left[\tilde{\boldsymbol{y}}_k - \boldsymbol{h}(\hat{\boldsymbol{x}}_k^-)\right] \tag{23}$$

$$\hat{\boldsymbol{P}}_k^+ = \left[\boldsymbol{I} - \boldsymbol{K}_k\boldsymbol{H}_k(\hat{\boldsymbol{x}}_k^-)\right]\hat{\boldsymbol{P}}_k^-\left[\boldsymbol{I} - \boldsymbol{K}_k\boldsymbol{H}_k(\hat{\boldsymbol{x}}_k^-)\right]^T + \boldsymbol{K}_k\boldsymbol{R}_k\boldsymbol{K}_k^T. \tag{24}$$

Note that the Joseph form[21] of the covariance update equation is used to improve numerical stability.

State Dynamics For estimating the sun heading vector the state of the system is given by

$$\boldsymbol{x} = \left[C\ {}^{\mathcal{B}}\boldsymbol{s}\right] \tag{25}$$

where C is a gross proportionality constant given by Equation (3) common to all CSS, smaller individual variations between sensors are assumed to be incorporated into the measurement noise model, and ${}^{\mathcal{B}}\boldsymbol{s}$ is the sun direction unit vector in the spacecraft body frame. The proportionality constant has been included in the state vector because it and the sun direction unit vector appear as a linear combination in the measurement equation. By imposing a unit length constraint on the state vector the sun heading estimate can easily be extracted from the state vector assuming the proportionality constant is nonzero.

The time derivative of the sun direction unit vector is found by solving

$$\frac{{}^{\mathcal{N}}\mathrm{d}}{\mathrm{d}t}\left({}^{\mathcal{B}}\boldsymbol{s}\right) = \frac{{}^{\mathcal{B}}\mathrm{d}}{\mathrm{d}t}\left({}^{\mathcal{B}}\boldsymbol{s}\right) + {}^{\mathcal{B}}\boldsymbol{\omega} \times {}^{\mathcal{B}}\boldsymbol{s} + \boldsymbol{\eta_s} \tag{26}$$

where $\boldsymbol{\eta_s}$ is zero-mean Gaussian noise. Assuming for time scales of interest the inertial sun vector is constant $\frac{{}^{\mathcal{N}}\mathrm{d}}{\mathrm{d}t}\left({}^{\mathcal{B}}\boldsymbol{s}\right) \approx 0$ the state dynamics and process noise functions are written as

$$\boldsymbol{f}(\boldsymbol{x}, \boldsymbol{u}, t) = C\ {}^{\mathcal{B}}\boldsymbol{s} \times {}^{\mathcal{B}}\boldsymbol{\omega} \tag{27}$$

$$\boldsymbol{g}(\boldsymbol{x}, \boldsymbol{w}, t) = -\boldsymbol{\eta_s}. \tag{28}$$

Measurement Model Similar to Equation (2) the output voltage of the ith CSS is assumed to be given by

$$V_i = C\left(\boldsymbol{n}_i \cdot \boldsymbol{s}\right) + \eta_i \tag{29}$$

where the proportionality constant C is included to account for large scale variations across all CSS, for instance due to improper calibration, and small scale individual variations are treated as noise and captured in η_i. It is also assumed that for this problem the spacecraft is not aware of its position relative to the Earth and cannot calculate the expected input for each CSS due to Earth's albedo. Even though this noise is distinctly non-Gaussian and represents an unmodeled signal the EKF, as shown later, is still capable of converging. The measurement equation can thus be written as

$$\boldsymbol{h}(\boldsymbol{x}_k) = \begin{bmatrix} C\left(\boldsymbol{n}_1 \cdot \boldsymbol{s}\right) \\ \vdots \\ C\left(\boldsymbol{n}_N \cdot \boldsymbol{s}\right) \end{bmatrix} \tag{30}$$

where N is the number of CSS. The discrete-time measurements from the ith coarse sun sensors are given simply by

$$\tilde{y}_{i_k} = V_i. \tag{31}$$

Update and Propagation Taking the partial derivatives specified in the formulation of the EKF, specifically those in Equations (20) and (21), results in

$$\boldsymbol{F} = -\left[{}^{\mathcal{B}}\boldsymbol{\omega}\right]_\times, \quad \boldsymbol{G} = -\left[I\right]_{3\times 3} \tag{32}$$

where $[\cdot]_\times$ represents the skew-symmetric cross product matrix given by

$$[\boldsymbol{\sigma}]_\times = \begin{bmatrix} 0 & -\sigma_3 & \sigma_2 \\ \sigma_3 & 0 & -\sigma_1 \\ -\sigma_2 & \sigma_1 & 0 \end{bmatrix}$$

and

$$\boldsymbol{H}_k(\hat{\boldsymbol{x}}_k^-) = \begin{bmatrix} \boldsymbol{n}_1^T \\ \vdots \\ \boldsymbol{n}_N^T \end{bmatrix}. \tag{33}$$

Examining Equations (32) and (33), it is seen that both the state dynamics and the measurement equation are linear, thus

$$\dot{\boldsymbol{x}} = \boldsymbol{F}\boldsymbol{x} + \boldsymbol{G}\boldsymbol{w} \tag{34}$$

$$\tilde{\boldsymbol{y}}_k = \boldsymbol{H}\boldsymbol{x}_k + \boldsymbol{v}_k \tag{35}$$

or

$$\dot{\boldsymbol{x}} = -\left[\boldsymbol{\omega}\right]_\times \boldsymbol{x} - \left[I\right]_{3\times 3} \boldsymbol{\eta_s} \tag{36}$$

$$\tilde{\boldsymbol{y}}_k = \begin{bmatrix} \boldsymbol{n}_1^T & \cdots & \boldsymbol{n}_N^T \end{bmatrix}^T \boldsymbol{x}_k + \boldsymbol{\eta}_k. \tag{37}$$

As a result the linearization used in the derivation of the EKF is not necessary and the filter is identical to a traditional Kalman filter.

Observability Since it has been shown that the system is linear, the observability of the system is determined using linear systems theory. For a continuous linear time-varying system the observability Gramian is given by[22]

$$\boldsymbol{M}\left(t_f, t_0\right) = \int_{t_0}^{t_f} \boldsymbol{\Phi}^T\left(t, t_0\right) \boldsymbol{H}^T \boldsymbol{H} \boldsymbol{\Phi}\left(t, t_0\right) dt \tag{38}$$

where the state transition matrix $\boldsymbol{\Phi}\left(t, t_0\right)$ must satisfy

$$\dot{\boldsymbol{\Phi}}\left(t, t_0\right) = \boldsymbol{F}\left(t\right) \boldsymbol{\Phi}\left(t, t_0\right) \tag{39}$$

with initial conditions

$$\boldsymbol{\Phi}\left(t_0, t_0\right) = \boldsymbol{I}. \tag{40}$$

The system is observable if and only if $\boldsymbol{M}\left(t, t_0\right)$ is invertible for some t. It is easily shown for any time history of angular velocities and for any orientation of the sun relative to the spacecraft the observability Gramian has rank equal to three and is invertible.

This EKF method is attractive as it uses a time history of measurements to improve its estimate instead of using only measurements from a single point in time. In addition, while the single-point algorithms discussed previously incorporate only those sensors that report a measurement, by propagating the state equations the EKF is able to account for sensors that are predicted to have output but are not registering any input irradiance.

Angular Velocity Estimate

The control used to reorient the spacecraft to a power positive state requires a measure of the spacecraft's angular velocity in order to arrest any rates. In addition, while the deterministic single-point methods do not incorporate the spacecraft's angular velocity, the EKF method does require an estimate of the vehicle's angular rates in order to propagate the system dynamics. Nominally, the angular velocity of the spacecraft is provided by a rate gyroscope, usually embedded within an

inertial measurement unit. However, in a power critical situation it may be necessary to turn off the inertial measurement unit. For this situation, a simple estimate of the vehicle's angular velocity vector is developed using the two most recent estimates of the sun direction unit vector.

By taking the cross product of the current and previous estimates of the sun direction vector, an estimate of the direction of the body angular velocity vector $\bar{\boldsymbol{\omega}}$ is determined. This is then scaled by the angle between the two vectors and divided by the time since the previous sun direction vector estimate to provide an estimate of the body angular velocity vector.

$$\bar{\boldsymbol{\omega}}_k = \frac{{}^{\mathcal{B}}\hat{\boldsymbol{s}}_k \times {}^{\mathcal{B}}\hat{\boldsymbol{s}}_{k-1}}{\|{}^{\mathcal{B}}\hat{\boldsymbol{s}}_k \times {}^{\mathcal{B}}\hat{\boldsymbol{s}}_{k-1}\|} \frac{\cos^{-1}\left({}^{\mathcal{B}}\hat{\boldsymbol{s}}_k \cdot {}^{\mathcal{B}}\hat{\boldsymbol{s}}_{k-1}\right)}{t_k - t_{k-1}} \tag{41}$$

In Equation (41) ${}^{\mathcal{B}}\hat{\boldsymbol{s}}_k$ is the best estimate of the sun direction unit vector in the body frame at time t_k. Note that with this rate estimate formulation it is not possible to estimate the full three-dimensional $\boldsymbol{\omega}$ vector as rates about ${}^{\mathcal{B}}\hat{\boldsymbol{s}}$ are not observable. However, for the purpose of coarse sun pointing this is not an issue, as such rotations about the sun direction vector will not impact the solar panel incidence angle or the associated electrical power generation.

Results, shown later, show that even though this method does not provide any new information it does provide an estimate adequate to achieve a power positive orientation. Because the estimate of the spacecraft's angular velocity vector is found through differentiation it is expected the amount of noise in the estimate will increase. To counteract this, the estimate is conservatively bounded about each axis and run through a first order low-pass filter. The numerical simulation shown next assumes maximum initial angular rates of 2.0 deg/sec about each axis so the bound on the angular rate estimate about each axis is set conservatively at 10 deg/sec which was shown in testing to provide the best performance.

NUMERICAL SIMULATION

An initially uncontrolled tumbling spacecraft is simulated to demonstrate the performance of the various methods discussed previously in estimating the sun heading and orienting the spacecraft in a power positive attitude. The spacecraft is modeled in a 400 km altitude circular orbit with an inclination of 90 deg starting on 2013 June 1, 00:00 UTC. For this orbit the spacecraft has a period of approximately 92.5 minutes and spends approximately 56.6 minutes in view of the Sun per orbit. The relative positions of the Earth and Sun are simulated using ephemeris from the NASA Navigation and Ancillary Information Facility (NAIF) SPICE toolkit.[23]

Spacecraft Parameters

The spacecraft is assumed to have a diagonal inertia matrix given by

$$[I] = \begin{bmatrix} 10.5 & 0 & 0 \\ 0 & 8 & 0 \\ 0 & 0 & 6.75 \end{bmatrix} \text{ kg m}^2.$$

Additionally, the spacecraft is assumed to have four reaction wheels and three magnetic torque bars which are used by the control algorithm. In the spacecraft body frame the spin, or alignment, axes for these devises are

$$[G_s] = \begin{bmatrix} 0 & 0 & \cos(45^\circ) & -\cos(45^\circ) \\ \cos(45^\circ) & \sin(45^\circ) & -\sin(45^\circ) & -\sin(45^\circ) \\ \sin(45^\circ) & -\cos(45^\circ) & 0 & 0 \end{bmatrix}, \quad [G_t] = \begin{bmatrix} 1 & 0 & 0 \\ 0 & 1 & 0 \\ 0 & 0 & 1 \end{bmatrix}.$$

Table 1: Control gains used for numerical simulation

$[K]$	$[P]$	$[K_I]$	c
$0.148\boldsymbol{I}_{3\times3}$ Nm	$0.9\boldsymbol{I}_{3\times3}$ Nms	$0.0001\boldsymbol{I}_{3\times3}$ $\text{N}^{-1}\text{s}^{-2}$	0.005 s^{-1}

Each reaction wheel is assumed to have a spin-axis inertia of $J_s = 0.001\,\text{kgm}^2$ and a maximum torque of 30 mNm. The torque bars are assumed to have a maximum dipole of $20\,\text{Am}^2$.

The spacecraft's initial true anomaly and attitude are uniformly distributed amongst all possible values and its initial angular velocity is uniformly distributed about all three axes with a maximum value of 2.0 deg/sec. Angular rate measurements are simulated at 10.0 Hz assuming a Gaussian distributed constant bias with a standard deviation of 1 deg/hr and white Gaussian noise with a standard deviation of 0.01 deg/sec.

CSS measurements are simulated at 10 Hz and the alignment of each CSS is varied normally about all three axes by an angle with a standard deviation of 1.0 deg. The warping shown in Figure 2 is applied to each sensor and the output of each sensor is individually reduced by up to 5%, uniformly distributed, to simulate on-orbit degradation of sensors.

Control Algorithm

A nonlinear three-axis attitude control is used in the numerical simulation to reorient the spacecraft using redundant reaction wheels.[24] This control law is designed for detumbling and continuous autonomous momentum dumping, and its goal is to orient the spacecraft body frame $\mathcal{B}$ with a reference frame $\mathcal{R}$ where the attitude error between the body and reference frames is described using the Modified Rodrigues Parameter (MRP) set $\boldsymbol{\sigma}_{\mathcal{BR}}$. The reference attitude is assumed time-varying so the spacecraft must track the angular velocity of the reference frame $\boldsymbol{\omega}_r$. The control law is given by

$$\begin{aligned}[G_s]\,\boldsymbol{u}_s = &-[I]\left(\dot{\boldsymbol{\omega}}_r - [\boldsymbol{\omega}]_\times\,\boldsymbol{\omega}_r\right) + K\boldsymbol{\sigma}_{\mathcal{BR}} + [P]\,\delta\boldsymbol{\omega} + [P]\,[K_I]\,\boldsymbol{z} \\ &-\left([\boldsymbol{\omega}_r]_\times - [[K_I]\,\boldsymbol{z}]_\times\right)\left([I]\,\boldsymbol{\omega} + [G_s]\,\boldsymbol{h}_s\right) + \boldsymbol{L}\end{aligned} \tag{42}$$

where $\delta\boldsymbol{\omega} = \boldsymbol{\omega} - \boldsymbol{\omega}_r$, K is a scalar gain, $[K_I]$ is a gain matrix, $\boldsymbol{z}$ is the integral term, and $[P]$ is a positive definite gain matrix.

The control is proven to be asymptotically stabilizing and guarantees if $\boldsymbol{\sigma}$ converges to zero so will $\delta\boldsymbol{\omega}$. For further discussion of this control law and its development the reader is referred to Reference 24. For this numerical simulation the control gains specified in Table 1 are used and $\boldsymbol{\omega}_r = \dot{\boldsymbol{\omega}}_r = \begin{bmatrix}0 & 0 & 0\end{bmatrix}^T$. The control is implemented with a deadband of 15 deg; if the sun direction vector falls within 15 deg of the solar array unit vector the control is turned off.

Of importance to the implementation of this control law is the quantity $\boldsymbol{\sigma}_{\mathcal{BR}}$. The sun vector estimation algorithm computes a value for the sun direction unit vector in the body frame, not an attitude error. An error MRP is formed by finding the principal rotation vector necessary to rotate the sun direction vector ${}^{\mathcal{B}}\boldsymbol{s}$ to align with the solar array unit vector $\boldsymbol{c}$ expressed in the body frame. This vector is then used in the definition of the MRP vector

$$\boldsymbol{\sigma} = \hat{\boldsymbol{e}}\tan\left(\frac{\Phi}{4}\right) \tag{43}$$

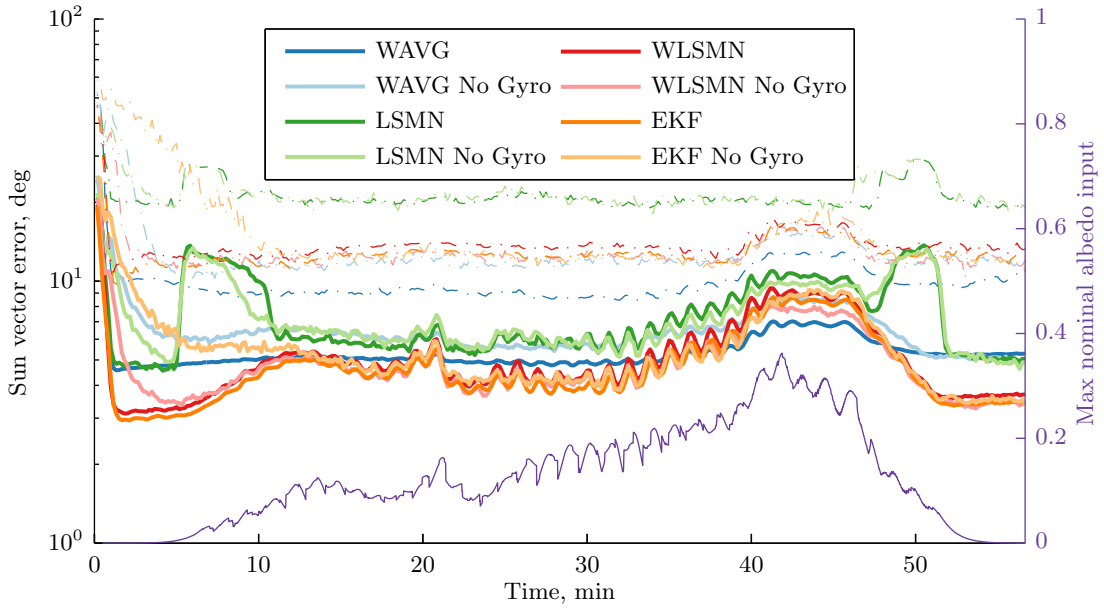

Figure 7: Statistics from 1000 case Monte Carlo analysis detailing the angular difference between the true sun direction and the estimate found using various methods with and without rate gyro measurements. Mean values are shown as solid lines and dashed lines indicate 95th percentile values. Maximum albedo input for all CSS during a nominal run is shown for comparison.

to create an error MRP. The equation for the error MRP is thus given by

$$\boldsymbol{\sigma}_{\mathcal{BR}} = \frac{{}^{\mathcal{B}}\boldsymbol{s} \times {}^{\mathcal{B}}\boldsymbol{c}}{\|{}^{\mathcal{B}}\boldsymbol{s} \times {}^{\mathcal{B}}\boldsymbol{c}\|} \tan\left(\frac{1}{4}\cos^{-1}\left({}^{\mathcal{B}}\boldsymbol{c} \cdot {}^{\mathcal{B}}\boldsymbol{s}\right)\right). \tag{44}$$

Equation (44) can result in a singularity when the denominator ${}^{\mathcal{B}}\boldsymbol{s} \times {}^{\mathcal{B}}\boldsymbol{c}$ approaches zero, or the solar array normal approaches alignment with the sun direction vector. However, as the value of the denominator goes to zero, so will the quantity ${}^{\mathcal{B}}\boldsymbol{c} \cdot {}^{\mathcal{B}}\boldsymbol{s}$. By simply setting the control to zero when the quantity ${}^{\mathcal{B}}\boldsymbol{c} \cdot {}^{\mathcal{B}}\boldsymbol{s}$ falls below a threshold, or deadband, this issue is avoided.

Results

The angular errors of the sun vector direction vector estimates for a 1000 case Monte Carlo analysis are shown in Figure 7. All four methods are simulated twice, once with angular velocity measurements from a rate gyroscope and once without. The maximum value of the CSS input due to Earth albedo for a nominal orbit is shown for comparison. The total vehicle angular velocity of the spacecraft is shown in Figure 8. In all plots both the mean and 95th percentile values are shown as solid and dashed lines, respectively.

All four methods successfully reorient the spacecraft to well below the requirement of 30 degrees, aligning the solar array unit normal with the sun direction vector. The input due to Earth albedo is expected to be the largest error source and this correlates well as all four methods show an error profile with a strong resemblance to the maximum input seen in a nominal orbit due to Earth albedo. Unlike the other methods, the LSMN method exhibits two large spikes near the beginning and end of the spacecraft's time in view of the Sun. The least squares method is known to be sensitive to

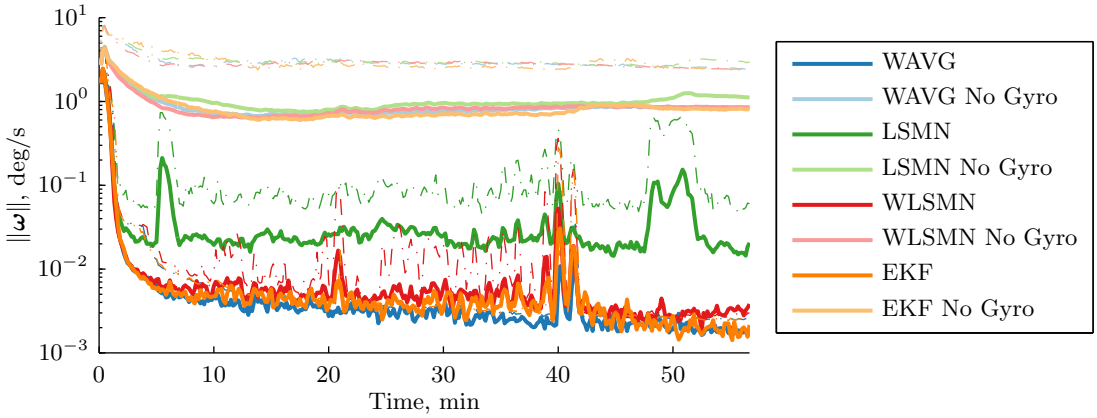

Figure 8: Magnitude of angular rate statistics from 1000 case Monte Carlo analysis for all four methods with and without rate gyro measurements. Mean values are shown as solid lines and 95th percentile values as dashed lines.

outliers and the two spikes seen correspond to when the ratio of measured CSS values is large. This typically occurs when several sensors are pointed directly at the Sun and one or two sensors receive relatively small input due to Earth's albedo.

As shown in Figure 7, the EKF and WLSMN methods exhibit the best accuracy both with and without angular velocity measurements. Within one orbit the two methods converge to an average error of approximately 3.5 deg with and without rate measurements. The WAVG and LSMN methods both converge to an average error of approximately 5 deg with and without rate measurements. The weighted average results correlate well with Figure 5. The average knowledge error seen corresponds to an an attitude error of 10 deg and the 95th percentile knowledge error corresponds to an attitude error of approximately 15 deg which is equal to the controller deadband.

With rate gyroscope measurements three of the four methods are shown to drive the spacecraft's angular velocity to the noise level. The LSMN method does show a slightly higher residual angular rate. As noted previously, the LSMN shows poor performance when the ratio of measured CSS values is large, which typically occurs when the input due to Earth's albedo is small. At these times, the estimate of the sun heading vector often exceeds the 15 deg deadband causing the controller to actively rotate the spacecraft. Since the initial true anomaly is uniformly distributed for all cases, these instances of active control cause, in aggregate, the mean angular velocity to be higher than the noise level. In all cases the angular velocity used in the filter is passed through a 0.1 Hz low pass filter, and this filtering is the reason the angular velocities take a finite time to drop to the noise level. This filter frequency is selected to reduce the noise in the signal without exciting any unmodeled structural modes.

Without angular velocity measurements all estimate techniques perform similarly well, in conjunction with the controller, bringing the vehicle's angular rates down to approximately 1.0 deg/sec. In all cases the residual angular velocity is about the body z axis. This is expected as it was noted earlier that the angular velocity estimate used is unable to observe rates about the sun heading vector and the goal of the controller is to orient this axis with the body z axis.

Of more practical importance is how fast the algorithms in question can reorient the spacecraft to a power positive orientation. It is important to note that the spacecraft is estimating the sun

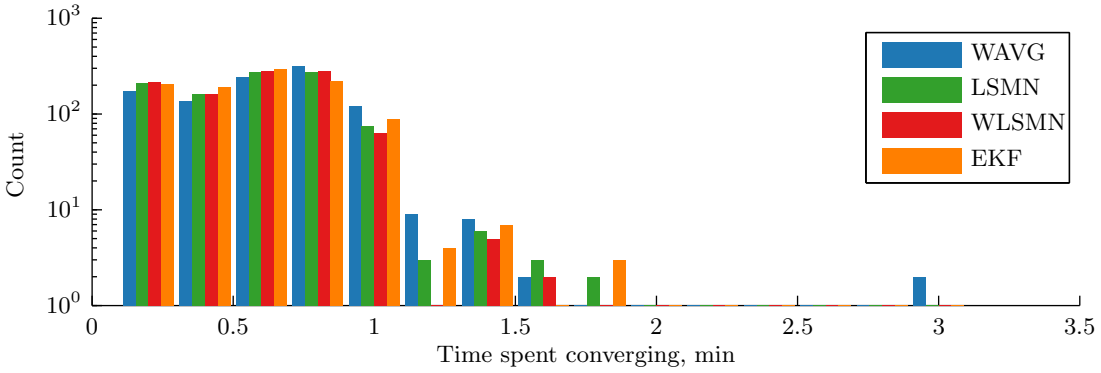

(a) With rate gyro measurements.

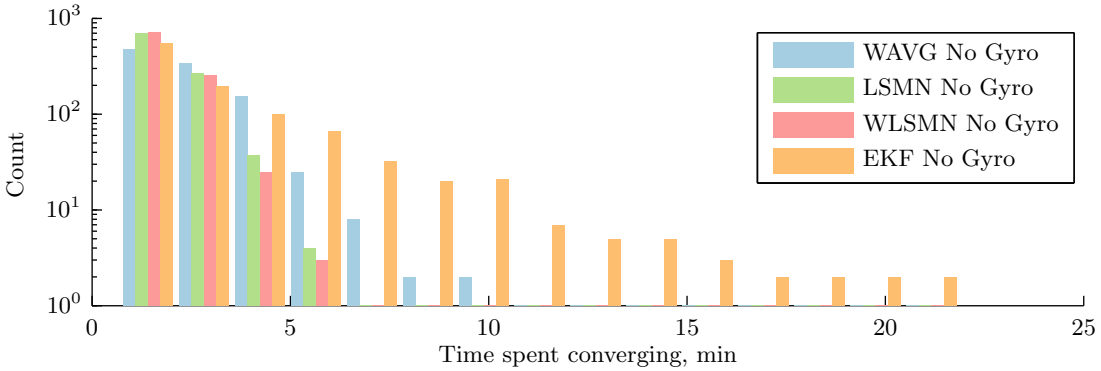

(b) Without rate gyro measurements.

Figure 9: Time spent converging, i.e. spacecraft solar arrays not pointed within 30 deg of sun vector, for 1000 Monte Carlo simulation cases with and without angular velocity measurements.

direction vector, and controlling its attitude based on that estimation at the same time, from the start of the simulation; the control does not wait for estimator convergence to act. Also, in a single orbit the spacecraft may be required to reorient up to two times: the first time the spacecraft senses the sun and again when coming out of the shadow of the Earth. While all cases converged to a power positive orientation, some take longer than others. The total time spent converging, i.e. the amount of time the solar arrays are not pointed within 30 deg of the sun, for each of the four cases is shown in Figure 9.

All four methods show similar performance when angular velocity measurements are available spending less than 3 minutes converging. The WLSMN exhibits the lowest maximum time spent converging, 1.5 min, and the WAVG method shows the highest with one case that takes 3 min to converge.

Significantly more variation is seen between the methods when no angular velocity measurements are used. In these cases the larger error in angular velocity of the spacecraft can lead to slow tumbling when in the shadow of the Earth that must be corrected once CSS measurements are available again. In addition, the EKF method relies on accurate angular velocity values to propagate the system equations and errors in the spacecraft's angular velocity lead to increased convergence

time. The LSMN and WLSMN methods exhibit the best performance taking at most 5.17 min to converge. The WAVG takes at most 8.5 min and the EKF method shows the poorest performance taking up to 21.17 min to converge. With the EKF the errors in the angular velocity delay the convergence of the estimate, however, as the EKF accumulates measurements over time it successfully converges and drives down the sun pointing error.

CONCLUSIONS

Four methods, WAVG, LSMN, WLSMN, and EKF, for estimating and controlling a spacecraft's orientation relative to the Sun using only minimal coarse sun sensors are presented. The first method uses a simple weighted average calculation, the second and third involve variations on a combination of least squares and minimum norm criteria, and the fourth incorporates an extended Kalman filter. The estimation methods are used in conjunction with a nonlinear three-axis controller to point the spacecraft's solar arrays at the Sun. All four methods are shown to be capable of successfully reorienting a spacecraft from any initial orientation in a reasonable time frame despite the presence of measurement noise. In addition, all methods are robust to uncertainties in the level of solar irradiance seen on-orbit reducing the complexities and costs of CSS ground-testing prior to launch.

The weighted average method is attractive because it is computationally simple, but it provides the least accurate steady state sun direction estimate. The least squares minimum norm solution is shown to be highly sensitive to large scale differences between CSS measurements, caused by the difference in voltage output for direct sunlight and Earth albedo reflected light, but a simple weighting scheme, used in the WLSMN method, is shown to alleviate these issues. The EKF method provides the most accurate estimate of the sun direction vector and utilizes measurements over time to create a more robust estimate, but takes longer to converge when lacking angular velocity measurements. Future research will have to evaluate what impact sensor failure has on the performance of all four methods. Even without angular velocity measurements, all four methods are shown to bring the spacecraft to a power positive orientation in a timescale much less than one full orbit thus providing a low cost, low power, coarse sun sensor only solution to reorienting a spacecraft following deployment.

REFERENCES

[1] Puig-Suari, J., Turner, C., and Twiggs, R. J., "CubeSate: The Development and Launch Support Infrastructure for Eighteen Different Satellite Customers on One Launch," *Proceedings of the AIAA/USU Conference on Small Satellites*, Logan, UT, 2001, ISBN 6507238651, pp. 1–5.

[2] Bouwmeester, J. and Guo, J., "Survey of worldwide pico- and nanosatellite missions, distributions and subsystem technology," *Acta Astronautica*, Vol. 67, No. 7-8, Oct. 2010, pp. 854–862, ISSN 00945765, 10.1016/j.actaastro.2010.06.004.

[3] Rufino, G., Grassi, M., and Rolfi, M., "Preliminary Calibration Results For a High-Precision CMOS Sun Sensor," *Proceedings of the AIAA Guidance, Navigation, and Control Conference and Exhibit*, No. August 2008, Honolulu, HI, Aug. 2011, pp. 1–9.

[4] Ninomiya, K., Ogawara, Y., Tsuno, K., and Akabane, S., "High Accuracy Sun Sensor Using CCDs," *Proceedings of the AIAA Guidance, Navigation, and Control Conference*, American Institute of Aeronautics and Astronautics, Minneapolis, MN, 1988.

[5] Black, H. D., "A Passive System for Determing the Attitude of a Satellite," *AIAA Journal*, Vol. 2, No. 7, 1964, pp. 1350–1351.

[6] Davenport, P. B., "A Vector Approach to the Algebra of Rotations with Applications," Tech. Rep. August, National Aeronautics and Space Adminstration, Goddard Space Flight Center, Greenbelt, MD, 1968.

[7] Shuster, M. D. and Oh, S. D., "Three-Axis Attitude Determination from Vector Observations," *Journal of Guidance, Control, and Dynamics*, Vol. 4, No. 1, 1981, pp. 70–77.

[8] Markley, F. L., "Attitude Determination Using Vector Observations: A Fast Optimal Matrix Algorithm," *Journal of the Astronautical Sciences*, Vol. 41, No. 2, 1993, pp. 261–280.

[9] Mortari, D., Markley, F. L., and Singla, P., "Optimal Linear Attitude Estimator," *Journal of Guidance, Control, and Dynamics*, Vol. 30, No. 6, Nov. 2007, pp. 1619–1627, ISSN 0731-5090, 10.2514/1.29568.

[10] Appel, P., "Attitude Estimation from Magnetometer and Earth-Albedo-Corrected Coarse Sun Sensor Measurements," *Acta Astronautica*, Vol. 56, No. 1-2, Jan. 2005, pp. 2–5.

[11] Jung, H. and Psiaki, M. L., "Tests of Magnetometer/Sun-Sensor Orbit Determination Using Flight Data," *Proceedings of the AIAA Guidance, Navigation, and Control Conference and Exhibit*, No. August, American Institute of Aeronautics and Astronautics, Montreal, Canada, Aug. 2001.

[12] Kalman, R. E., "A New Approach to Linear Filtering and Prediction Problems," *Journal of Basic Engineering*, Vol. 82, No. Series D, 1960, pp. 35–45.

[13] Julier, S. J., Uhlmann, J. K., and Durrant-Whyte, H. F., "A New Approach for Filtering Nonlinear Systems," *Proceedings of the American Control Conference*, Vol. 3, No. 3, 1995, pp. 1628–1632, 10.1109/ACC.1995.529783.

[14] Jackson, B. and Carpenter, B., "Optimal Placement of Spacecraft Sun Sensors Using Stochastic Optimization," *Proceedings of the IEEE Aerospace Conference*, IEEE, Big Sky, MT, Mar. 2004, ISBN 0780381556104, pp. 3916–3923.

[15] Springmann, J. C. and Cutler, J. W., "Optimization of Directional Sensor Orientation with Application to Photodiodes for Spacecraft Attitude Determination," *Proceedings of the AAS/AIAA Space Flight Mechanics Conference*, Kauau, HI, Feb. 2013, pp. 1–19.

[16] Lerner, G. M., *Spacecraft Attitude Determination and Control*, chap. Sun Sensors, D. Reidel Publishing Co., Dordrecht, The Netherlands, 1978, pp. 155–166.

[17] Flatley, T. W. and Moore, W. A., "An Earth Albedo Model: A Mathematical Model for the Radiant Energy Input to an Orbiting Spacecraft Due to the Diffuse Reflectance of Solar Radiation From the Earth Below," Tech. rep., National Aeronautics and Space Administration, Goddard Space Flight Center, Greenbelt, MD, 1994.

[18] Bhanderi, D. D. V. and Bak, T., "Modeling Earth Albedo for Satellites in Earth Orbit," *Proceedings of the AIAA Guidance, Navigation, and Control Conference and Exhibit*, American Institute of Aeronautics and Astronautics, San Francisco, CA, Aug. 2005.

[19] Tapley, B., Schutz, B., and Born, G., *Statistical Orbit Determination*, Elsevier Academic Press, 2004, ISBN 9780126836301.

[20] Crassidis, J. L. and Junkins, J. L., *Optimal Estimation of Dynamic Systems*, Applied Mathematics & Nonlinear Science, Chapman and Hall/CRC, 2004.

[21] Bucy, R. S. and Joseph, P. D., *Filtering for Stochastic Processes*, John Wiley & Sons, Inc., New York, 1968.

[22] Brogan, W. L., *Modern Control Theory*, Prentice Hall, 3rd ed., 1991.

[23] Acton, C., "Ancillary Data Services of NASA's Navigation and Ancillary Information Facility," *Planetary and Space Science*, Vol. 44, No. 1, 1996, pp. 65–70.

[24] Hogan, E. A. and Schaub, H., "Three-Axis Attitude Control using Redundant Reaction Wheels with Continuous Momentum Dumping," *Proceedings of the AAS/AIAA Spaceflight Mechanics Conference*, American Institute of Aeronautics and Astronautics, Kauai, HI, Feb. 2013.